

Eemian interglacial reconstructed from a Greenland folded ice core

NEEM community members*

Efforts to extract a Greenland ice core with a complete record of the Eemian interglacial (130,000 to 115,000 years ago) have until now been unsuccessful. The response of the Greenland ice sheet to the warmer-than-present climate of the Eemian has thus remained unclear. Here we present the new North Greenland Eemian Ice Drilling ('NEEM') ice core and show only a modest ice-sheet response to the strong warming in the early Eemian. We reconstructed the Eemian record from folded ice using globally homogeneous parameters known from dated Greenland and Antarctic ice-core records. On the basis of water stable isotopes, NEEM surface temperatures after the onset of the Eemian (126,000 years ago) peaked at 8 ± 4 degrees Celsius above the mean of the past millennium, followed by a gradual cooling that was probably driven by the decreasing summer insolation. Between 128,000 and 122,000 years ago, the thickness of the northwest Greenland ice sheet decreased by 400 ± 250 metres, reaching surface elevations 122,000 years ago of 130 ± 300 metres lower than the present. Extensive surface melt occurred at the NEEM site during the Eemian, a phenomenon witnessed when melt layers formed again at NEEM during the exceptional heat of July 2012. With additional warming, surface melt might become more common in the future.

A 2,540-m-long ice core was drilled during 2008–12 through the ice at the NEEM site, Greenland (77.45° N, 51.06° W, surface elevation 2,450 m, mean annual temperature -29°C , accumulation 0.22 m ice equivalent per year). The top 1,419 m is from the current interglacial, the Holocene, and together with the glacial ice below it can be matched to the NGRIP GICC05 extended timescale^{1,2} down to 2,206.7 m (108 thousand years before present, referred to as kyr BP, where 'present' is defined as AD 1950). Below this, the ice is disturbed and folded, but it contains zones with relatively high stable isotope values of H_2O ($\delta^{18}\text{O}_{\text{ice}}$, a proxy for condensation temperature), indicating that it stems from the last interglacial, the Eemian (130–115 kyr BP; Fig. 1). Near bedrock, low $\delta^{18}\text{O}_{\text{ice}}$ values suggest that the ice layers are most probably from the glacial period before the Eemian. The lowest 5 m of the ice core contain accreted ice, with dark layers 1–20 cm thick that contain high concentrations of basal material. In this study, information from the Eemian period of the NEEM ice core will be used to constrain the surface elevation of the ice sheet and the temperature of this warm climate period. Measurements of $\delta^{18}\text{O}_{\text{ice}}$ have been made, and air bubbles trapped within the ice have yielded concentrations of CH_4 and N_2O , stable isotope values $\delta^{15}\text{N}$ of N_2 and $\delta^{18}\text{O}$ of O_2 ($\delta^{18}\text{O}_{\text{atm}}$), and total air content (see details in Supplementary Information). In addition, the rheology of the ice, radio echo sounding (RES) images and surface temperatures and ice temperatures are used in the interpretation.

Reconstruction of the climate record

Stratigraphic disruptions are identified from discontinuities of $\delta^{18}\text{O}_{\text{ice}}$ at depths of 2,209.60 m, 2,262.15 m, 2,364.45 m and 2,432.19 m. Corresponding shifts in gas concentrations are found at these depths, so the bubble enclosure process has not caused the expected depth offset for stratigraphic undisturbed ice (Fig. 1). Possible discontinuities below 2,432.19 m have not been investigated. The records of CH_4 concentrations and $\delta^{18}\text{O}_{\text{atm}}$ are also disturbed and are not identical with the globally-homogeneous signals documented at the nearby NGRIP ice core (which contains undisturbed stratigraphy

back to 123 kyr BP) or with the EDML Antarctic ice core (which reaches back more than 135 kyr BP)^{3–6}. Measurements of N_2O , $\delta^{15}\text{N}$ and air content in the NEEM ice below 2,200 m further confirm these discontinuities.

NEEM data reveal spikes in CH_4 and N_2O records between depths of 2,370 m and 2,418 m, which are too rapid to be explained by climatic variability and coincide with lower air content in the ice (Figs 1b, 2, 4, shaded areas, and Supplementary Fig. 6). These characteristics point to surface melting or wet surface conditions. Indeed, surface melting or percolating rain reduces the firn air content and allows *in situ* production of CH_4 and N_2O . This hypothesis is supported by results in the near-surface ice from the warmer south Greenland Dye3 ice core (Supplementary Fig. 9, mean annual temperature -21°C) and by measurements of noble gases over the NEEM spikes, which also support the hypothesis of melting surface layers (Supplementary Fig. 8). The lack of parallel variability in $\delta^{18}\text{O}_{\text{ice}}$, $\delta^{15}\text{N}$ or $\delta^{18}\text{O}_{\text{atm}}$ suggests that these parameters are uninfluenced by surface melting. The spikes occur in the warmest interval at the depositional location indicated by water isotopes ($\delta^{18}\text{O}_{\text{ice}} > -33\text{‰}$). The mean water isotope value over the past millennium is -33.6‰ at NEEM, and very few melt layers are found in the ice core before 1995⁷. During our NEEM field campaigns (2007–12), the mean surface air temperature in July reached -5.4°C (with annual mean values of $\delta^{18}\text{O}_{\text{firn}} > -33\text{‰}$; ref. 8), and studies with ice cores and snow pits show that episodic melt events occurred. Over the period 12–15 July 2012, an exceptional heat wave produced significant surface melt over 97% of the Greenland ice sheet, leaving a strong fingerprint at the NEEM site in the form of melt layers 5–6 cm thick at 50–70 cm below the surface.

For depths of 2,201.10–2,432.19 m, the NEEM records of $\delta^{18}\text{O}_{\text{atm}}$ and the subset of CH_4 values not corrupted by surface melting are matched with globally-homogeneous signals of these values observed from other ice cores^{6,9,10} (Supplementary Figs 4 and 5). For younger ice, the nearby NGRIP $\delta^{18}\text{O}_{\text{ice}}$ record is used as a reference temperature target for synchronization by assuming simultaneous abrupt

*Lists of participants and their affiliations appear at the end of the paper.

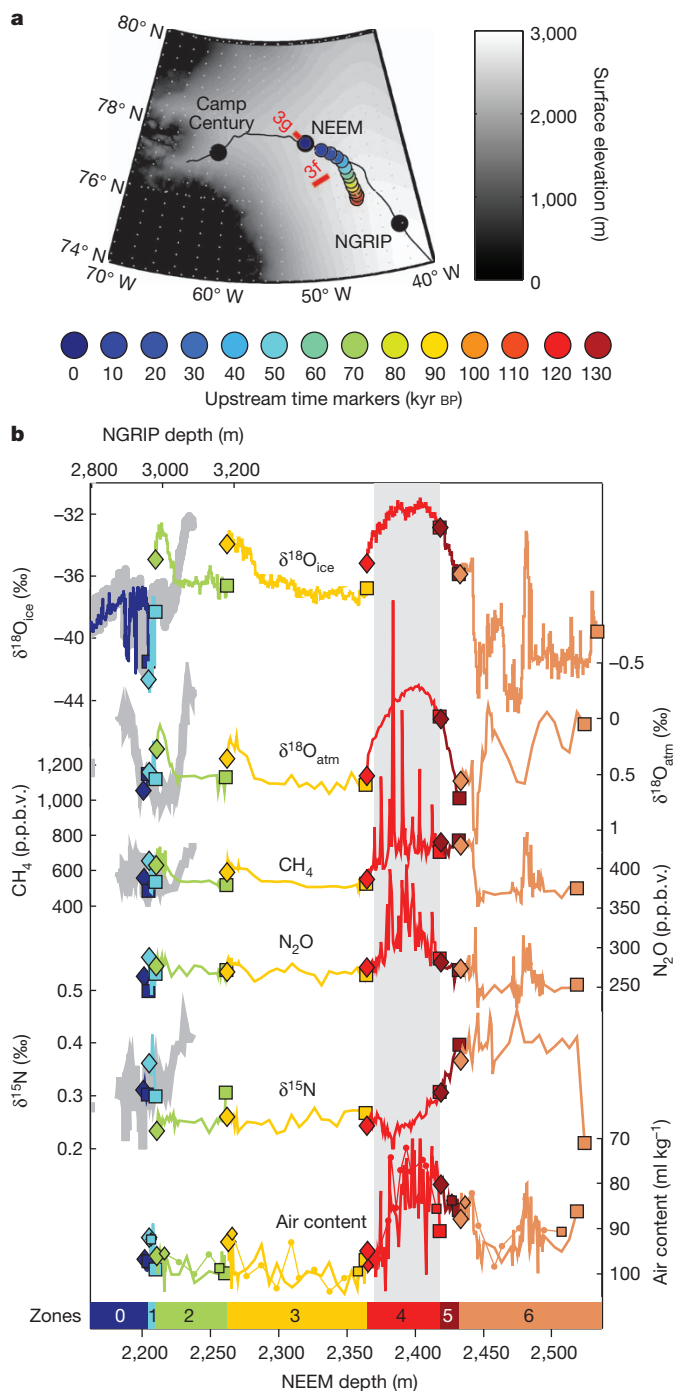


Figure 1 | Observed NEEM records. **a**, A surface elevation map (scale to the right) of the position of the NEEM camp, including coloured upstream depositional positions (upstream time marker scale below) of the ice found in the NEEM ice core. The deep ice-core sites NGRIP, NEEM and Camp Century and the tracks of the RES images shown in Fig. 3f and g (red lines) are shown on the map. **b**, The observed records of $\delta^{18}\text{O}_{\text{ice}}$, $\delta^{18}\text{O}_{\text{atm}}$ (reversed scale), CH_4 , N_2O , $\delta^{15}\text{N}$ and air content (reversed scale) from 2,162 m and deeper are plotted on the NEEM depth scale (bottom x axis). The air content measurements from LGGE and from University of Bern (thin curve, small symbols) are both included. Zones 0–6 (blue, 0–2,206.5 m; cyan, 2,206.5–2,209.6 m; green, 2,209.6–2,262.2 m; orange, 2,262.2–2,364.5 m; red, 2,364.5–2,418.0 m; dark red, 2,418.0–2,432.2 m; and brown, 2,432.2–2,537 m) represent the sections of the NEEM ice-core records with symbols marking the start (diamond) and end (square) of each zone. There is no discontinuity between zones 4 and 5 but spikes of CH_4 , N_2O and air content occur in zone 4 (shaded grey). For comparison, the NGRIP data are plotted as light grey curves on the NGRIP depth scale on top of the plot. The NEEM and NGRIP depth scale are synchronized between 2,162 and 2,207.6 m NEEM depths.

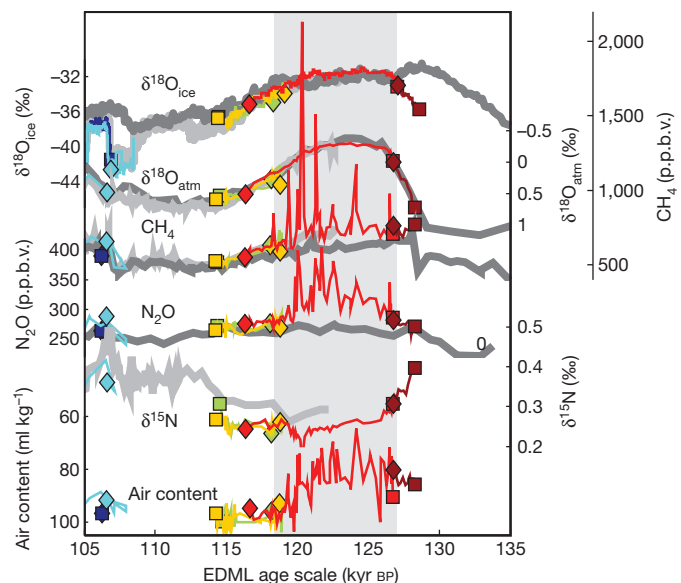


Figure 2 | Reconstructed records from the NEEM ice core. The reconstructed records of $\delta^{18}\text{O}_{\text{ice}}$, $\delta^{18}\text{O}_{\text{atm}}$ (reversed scale), CH_4 , N_2O , $\delta^{15}\text{N}$ and air content (reversed scale) on the EDML1 timescale¹². Zone 1 (cyan) is seen to contain a fold while zone 2 (green) and zone 3 (orange) are reversed and cover identical time periods. NGRIP records (light grey) and EDML records (dark grey) are included where they are available. The CH_4 , N_2O and air content records contain spikes from 127 to 118.3 kyr BP (shaded grey).

climate changes at the transitions between stadials and interstadials¹¹ (Supplementary Fig. 3).

In Fig. 2, the reconstructed NEEM records are shown on the EDML1 timescale¹² and compared to the NGRIP (light grey) and EDML (dark grey) records. Zones 1 to 5, identified in Fig. 1, map onto the timescale as coherent pieces. Zone 1 is folded such that the records are mirrored and repeated, zone 2 and zone 3 cover identical time periods, both inverted, while zone 4 (with melt-related spikes) and zone 5 are undisturbed and contain the major part of the ice from the Eemian (128.5–115 kyr BP) (Figs 2 and 3a, b). It cannot be ruled out that small disruptions or folds are present within the individual zones. The reconstructed records, however, show no unexpected discontinuities in either zones 1–5 or in all other measured parameters, such as $\delta^{15}\text{N}$ (Fig. 2), dust or electrical properties. As the timescale is transferred from the EDML ice core by matching it to the globally-homogeneous signals, small undetectable disruptions will not influence the conclusions based on the parameters presented here. The reconstruction is unambiguous and no other solution exists to match the NEEM $\delta^{18}\text{O}_{\text{atm}}$ and the uncorrupted CH_4 values simultaneously to the undisturbed EDML and NGRIP records. No ice from 114–108 kyr BP can be found in the NEEM ice core, while the ice layer from 118–115 kyr BP is found three times (zones 2, 3 and 4), two of which are inverted.

Northern Hemisphere temperatures are known to vary in parallel with the atmospheric CH_4 concentration^{13,14}, which is seen to increase abruptly into the warm Eemian period at 128 kyr BP at EDML. This is evidence that no substantial warm phases of the NEEM Eemian record are missing before 128.5 kyr BP. Ice from below 2,450 m (zone 6) appears to be too disturbed to reconstruct an age scale based on the data available at present. The very low (glacial) $\delta^{18}\text{O}_{\text{ice}}$ values (–44.9‰ at 2,476 m) are first found again in the record above 2,011 m. The ice layering at the NEEM site is undisturbed above 2,200 m (Fig. 3g), so the section below 2,476 m is believed to contain ice older than 128.5 kyr BP from Marine Isotopic Stage (MIS) 6, and we may speculate that the increased levels of $\delta^{18}\text{O}_{\text{ice}}$, CH_4 and N_2O at 2,480 m might be from MIS-7 interglacial.

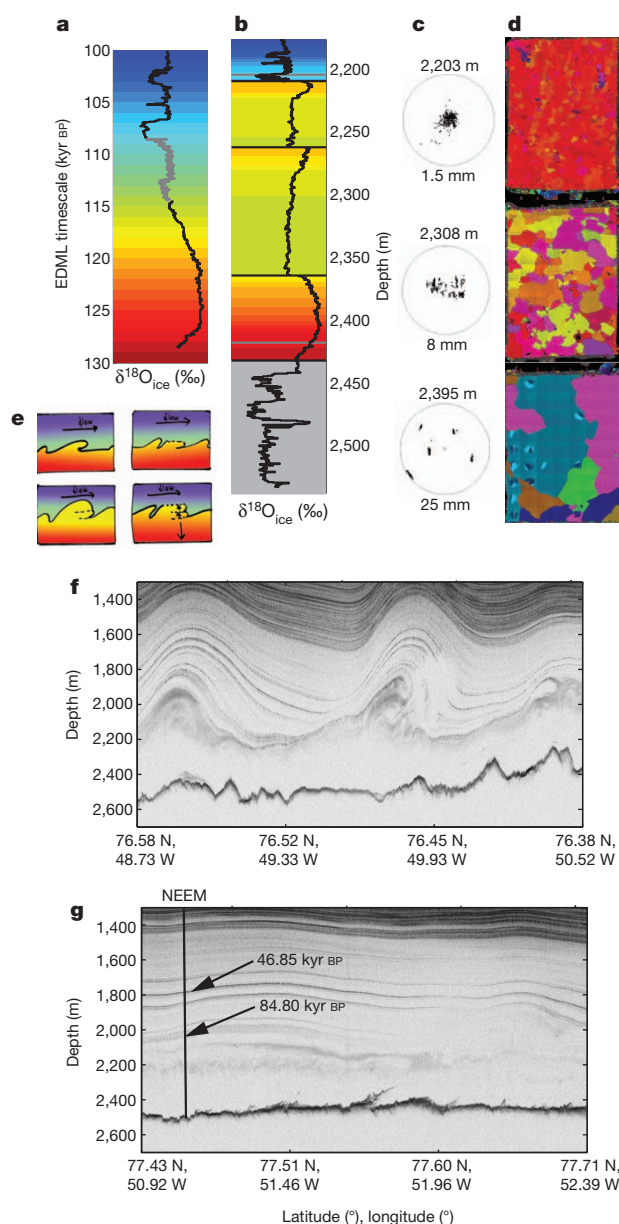


Figure 3 | Disturbances of the deep NEEM ice. **a**, The reconstructed NEEM water stable isotope record (black curve) including NGRIP data between 114–108 kyr BP (grey) on the EDML1 timescale that has been colour coded according to age. Below 2,432.19 m (grey shading) no dating has been attempted. **b**, The colour-coded data plotted with the original data on the NEEM depth scale visualizing the discontinuities and the reversed sections. **c**, **d**, c-Axis orientations on Schmidt diagrams for depths 2,203 m, 2,308 m and 2,395 m (**c**) and polarized light pictures of ice thin sections from the same three depths (**d**) demonstrate the very different ice rheology of the glacial and interglacial ice, leading to different flow properties. **e**, Cartoon of a possible history of the formation of two overturned folds at NEEM inspired by the observed undulations in the RES images (**f** and **g**). **f**, **g**, Center for Remote Sensing of Ice Sheets (CREGIS) ice-penetrating RES images from NASA Operation IceBridge campaign 2011. **f**, A 52-km-long line to the west that illustrates that overturning folds do occur (MCORDS: 20110329_02_020); **g**, a 48-km-long line crossing the deep drill site (MCORDS 20110329_02_028). The NEEM site is marked on the image, and two dated horizons are marked. More details can be found in Supplementary Information.

The disturbed and folded ice

RES data were collected in north Greenland during 2011 and 2012 with a multichannel coherent ice-penetrating radar depth sounder/imager^{15,16}. The RES images show continuous and undisturbed internal layers (isochrones) to a depth of about 2,200 m in the NEEM

region, which agrees with the ice-core observations¹⁷. Below 2,200 m, internal layers become fuzzy and less continuous: undulations and even overturned folds and shearing of basal material are observed (Fig. 3f, g, Supplementary Fig. 2b–e). The transition between clear and fuzzy layers often appears at the interface between ice from the glacial and Eemian periods. Very large differences in ice rheological properties are documented (Fig. 3c, d) between glacial ice (with crystal sizes of 1.5 mm and a strong preferred vertical c-axis orientation) and Eemian ice (with crystal sizes of 25 mm and multiple maxima fabrics). The viscosities of these two types of ice differ by a factor of 50–100 (refs 18–21), allowing glacial ice to deform very easily while the interglacial ice remains more rigid. The missing, folded and inverted parts of the ice are from the interface between the relatively rigid Eemian and the early glacial (118–106 kyr BP), supporting the idea that the glacial ice deforms over the harder Eemian ice. The broken record at 128.5 kyr BP can be explained by contrasting the deformation properties of the underlying ice from the previous glacial period and the Eemian ice. It should be noted that the discontinuous and folded structures of the GRIP and GISP2 ice cores also occur for ice older than 105 kyr (refs 9, 10). The consistency of the RES images and deep ice-core results at NEEM is a breakthrough result, and demonstrates that RES imaging can now be used to predict folded ice layering. This creates the potential for a systematic reconstruction of the Eemian Greenland ice-sheet layering from new RES imaging. Assimilation of such data in ice-sheet models may lead to much improved histories of the configuration of the ice sheet in the past, improving our ability to predict its future evolution.

Climate reconstruction from observed records

The reconstructed Eemian sequence (128.5–114 kyr BP, Fig. 2) allows for initial climate interpretations of this period. As mentioned above, the regular occurrence of melt features at 127–118.3 kyr BP is an indication of warmer temperatures at the depositional surface locations of the ice than the mean of the recent millennium at NEEM. This is independently confirmed by the decrease of $\delta^{15}\text{N}$ in this zone, which is indicative of $\sim 5^\circ\text{C}$ warmer mean annual firn temperatures at the depositional site^{22,23} (Supplementary Fig. 7). Between 128.5 kyr BP and 126.0 kyr BP, $\delta^{18}\text{O}_{\text{ice}}$ increases from -35‰ to -31.4‰ while EDML $\delta^{18}\text{O}_{\text{ice}}$ values slowly drop from those of the warm early Antarctic period²⁴. This bipolar see-saw behaviour suggests that inter-hemispheric heat redistribution by the Atlantic meridional overturning circulation²⁵ was taking place within the Eemian interglacial period; this has also been observed during the last Northern Hemisphere deglaciation 19–11 kyr BP^{24–27}. Before surface melt began between 128.5 and 126.7 kyr BP, the air content at the depositional site had a stable level of 85 ml kg^{-1} compared to the present level of 97.5 ml kg^{-1} . When corrected for changing local summer insolation^{28–30} (Supplementary Fig. 10), the air content difference suggests a surface elevation at the depositional site 540 \pm 300 m higher at the onset of the Eemian (128 kyr BP) than the surface elevation at NEEM today^{28,31–33}. The locations of the depositional sites of the Eemian ice found in the NEEM ice core are modelled using a nested three-dimensional flow model³⁴ (Fig. 1a and Supplementary Fig. 1). A second model used to date the NEEM ice core reaches similar locations³⁵ within 20 km. At present, the surface elevation at the depositional site of the 128-kyr-BP ice ($205 \pm 20\text{ km}$ upstream from NEEM) is $330 \pm 50\text{ m}$ higher than the present at NEEM^{33,34}. The surface elevation increase of $210 \pm 350\text{ m}$ at the 128-kyr-BP depositional site (Fig. 4c, blue) is the difference between the elevation at 128 kyr BP ($540 \pm 300\text{ m}$) and the present elevation ($330 \pm 50\text{ m}$), both related to the present elevation at NEEM. This surface elevation increase is expected at the onset of a warm climatic period due to increased precipitation and mass balance changes that occur before the central part of the ice sheet adjusts to the warmer climate by increasing the ice flow. This is also established at the onset of the present interglacial at 11.7 kyr BP³².

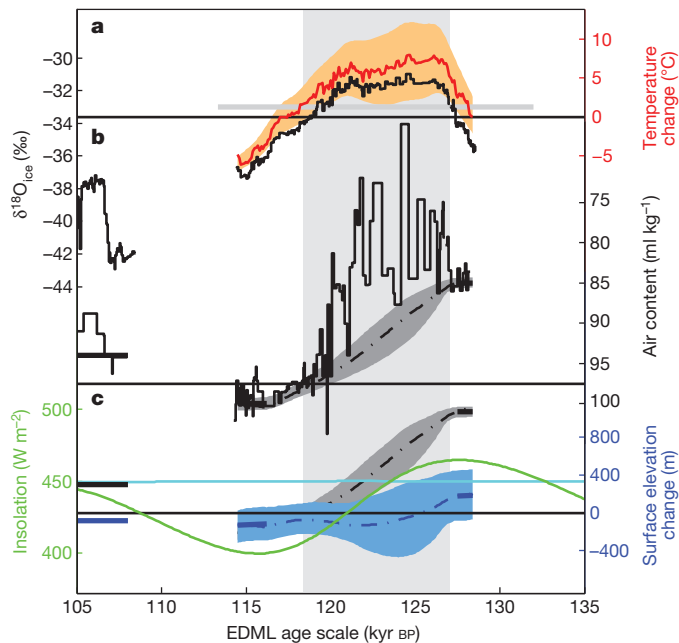


Figure 4 | Reconstruction of the temperature and elevation history.

Reconstruction of the temperature and elevation history through the Eemian based on the stable water isotopes ($\delta^{18}\text{O}_{\text{ice}}$) and the air content records. The zone with surface melt (127–118.3 kyr BP) is shaded in light grey. **a**, The measured $\delta^{18}\text{O}_{\text{ice}}$ record (black) on the constructed timescale. The average of the recent millennium (-33.60‰) is marked with a thin black line. It is seen that the $\delta^{18}\text{O}_{\text{ice}}$ values at the depositional locations in the melt zone are above -33.0‰ (grey horizontal line). The fixed-elevation change of temperature—constructed from the observed $\delta^{18}\text{O}_{\text{ice}}$, the elevation changes determined from the air content and the upstream corrections (curves below)—is shown as a red curve using the red axis. The standard error range (orange shading) is a sum of the error of the $\delta^{18}\text{O}_{\text{ice}}$ and the elevation change correction (Supplementary Information 1.1, equations (2) and (5) in Supplementary Information, Supplementary Table 2). **b**, Air content (black) is plotted and guided by the two stable levels on each side of the melt zone. A dot-dashed line connecting these levels has been suggested with an error range as the dark grey shaded area. The standard error range is a sum of the error assumed in the zone with surface melt (127–118.3 kyr BP) and the 1% error on the air content measurements (Supplementary Information section 1.4). In addition, the average level 107–105 kyr BP is marked with a horizontal black bar. The changes in the air content are caused by pressure changes due to changing surface elevation at the depositional sites and changes to the air trapping processes in the firm assumed to be controlled by the changing summer insolation^{28,32,49,50}. **c**, When corrected for upstream flow (cyan) and summer insolation changes (green), the air content curve can be ‘translated’ to elevation changes (blue, dashed) with the shaded zone indicating the uncertainty range introduced by this translation. Blue bars mark the air content of the ‘translated’ air content black bars. The standard error range is based on the error range of the air content (dark grey shaded area) and the additional standard errors from calculation of the elevation changes (equation (5) in Supplementary Information, and Supplementary Table 2).

In the period 127–118.3 kyr BP, the air content in the ice where surface melt occurred was highly variable and cannot directly be used for ice elevation reconstructions (Fig. 2, shaded zone). We can tentatively estimate elevation changes through the Eemian climate period by connecting the two air content levels before and after the melt zone (Fig. 4b) after correcting for summer insolation, which accounts for 50% of the observed change (Fig. 4c, Supplementary Information). At 126 kyr BP the surface elevation was 45 ± 350 m higher than at present. The $\delta^{18}\text{O}_{\text{ice}}$ increased to -31.4‰ at 126 kyr BP, exceeding the current mean value of the recent millennium of -33.6‰ (at the NEEM site) and the current mean value of -35.0‰ at the depositional site^{32,33} (Supplementary Information, section 2). Using the temperature–isotope relation of $2.1 \pm 0.5 \text{ K } \text{‰}^{-1}$ (calibrated using data from the present interglacial³²), the 3.6‰ anomaly at 126 kyr

BP implies that precipitation-weighted surface temperatures were $7.5 \pm 1.8 \text{ °C}$ warmer at the depositional site compared to the last millennium. Note that the modelled location of the depositional site is the only modelled parameter required to compare the 126-kyr-BP data to the present-day data at the depositional site. When further correcting for the more uncertain elevation change of 45 ± 350 m at the 126-kyr-BP depositional site using a lapse rate of $7.5 \pm 0.5 \text{ K km}^{-1}$, the fixed-elevation temperature increase here is $8 \pm 4 \text{ °C}$ (Fig. 4a, red). Our data depict a gradual cooling until 110 kyr BP (Fig. 4a, red curve).

The reconstructed precipitation-weighted annual temperature changes are remarkably high. In general, warmer summer temperatures are reported from palaeorecords^{36,37}, and a few find temperatures at 126 kyr BP on high Arctic latitudes as high as those reported from NEEM^{38–40}. Climate models equipped with water stable isotopes point to a limited (1 °C) seasonality bias caused by a stronger enhancement of temperature and precipitation in summer than in winter^{41–43}. A large spread in temperature has been reported among simulations of the last interglacial climate, which appear to systematically underestimate North Atlantic/Arctic warming, possibly due to missing vegetation and ice-sheet feedback^{37,42,43}.

Within 6,000 yr, from 128 to 122 kyr BP, the surface elevation is estimated to have decreased from 210 ± 350 m above to 130 ± 300 m below the present surface elevation, which translates to a moderate ice thickness change of 400 ± 350 m after accounting for isostatic rebound. Based on this estimate, the ice thickness at NEEM decreased by an average of 7 ± 4 cm per year between 128 and 122 kyr BP and stayed at this level until 117–114 kyr BP, long after surface melt stopped and temperatures fell below modern levels.

Even with minimum ice thickness of only about 10% less than the present ice thickness at the NEEM site, as reported here, substantial melting can cause significant reduction of ice thickness near the margins; this in turn reduces the volume of the Greenland ice sheet. Although the documentation of ice thickness at one location on the Greenland ice sheet cannot constrain the overall ice-sheet changes during the last interglacial period, the NEEM data can only be reconciled with Greenland ice-sheet simulations³⁰ that point to a modest contribution (2 m) to the observed 4–8 m Eemian sea level high stand^{44,45}. For comparison, no continuing elevation change has so far been detected in areas with elevations above 2,000 m in north Greenland during the past few decades⁴⁶. These findings strongly imply that Antarctica must have contributed significantly to the Eemian sea level rise⁴⁷.

Despite the complex ice flow, the disturbed record of the deep ice in the NEEM ice core can be unambiguously reconstructed. The anatomy of the last interglacial shows that Greenland temperatures peaked after the onset of the Eemian, 126 kyr BP, with temperatures (at fixed elevations) $8 \pm 4 \text{ °C}$ warmer than the average of the recent millennium and multiple indications of summer melt. Temperatures gradually decreased during the interglacial, very probably owing to the strong local summer insolation decreasing trend. The surface elevation first increased due to increased mass balance to 210 ± 350 m above the present at 128 kyr BP, then decreased to 130 ± 300 m below the present elevation around 122 kyr BP. Our results provide multiple new targets to constrain coupled climate/ice-sheet models. Our record, together with recent observations of rainfall and strong surface melting in July 2012 at NEEM, show that conditions are conducive to the start of melt layer formation at NEEM, with the 2010–12 mean annual surface temperatures $1\text{--}2 \text{ °C}$ above the 1950–80 average.

Our results have implications for both ice deformation near the bedrock and the response of the Greenland ice sheet to climate change. The combination of high-resolution RES data and NEEM glacial–interglacial ice layers brings new knowledge of the near-bed deformation of ice. We believe that the folding and disturbances we observe near the bed are strongly related to the rigid deformation properties of the interglacial ice. This offers an alternative explanation

for the large anomalies in RES profiles recently observed under both the Antarctic and Greenland ice sheets, which were previously attributed to refrozen basal water⁴⁸.

METHODS SUMMARY

Measurements of stable water isotopes in the ice ($\delta^{18}\text{O}_{\text{ice}}$) and CH_4 , N_2O concentrations and the isotopes $\delta^{15}\text{N}$ of N_2 and $\delta^{18}\text{O}_{\text{atm}}$ of O_2 , noble gases and the air content have been measured in the air extracted from the air bubbles in the ice, all using well-described methods. These measurements are presented in Supplementary Information section 1. Models calculating temperatures from water isotopes, elevation changes from air content, and temperature changes from $\delta^{15}\text{N}$ values have been calibrated using observations from the present interglacial.

Received 31 July; accepted 13 November 2012.

- Wolff, E. W., Chappellaz, J., Blunier, T., Rasmussen, S. O. & Svensson, A. Millennial-scale variability during the last glacial: the ice core record. *Quat. Sci. Rev.* **29**, 2828–2838 (2010).
- Svensson, A. *et al.* A 60 000 year Greenland stratigraphic ice core chronology. *Clim. Past* **4**, 47–57 (2008).
- Andersen, K. K. *et al.* High-resolution record of Northern Hemisphere climate extending into the last interglacial period. *Nature* **431**, 147–151 (2004).
- Barbante, C. *et al.* One-to-one coupling of glacial climate variability in Greenland and Antarctica. *Nature* **444**, 195–198 (2006).
- Schilt, A. *et al.* Glacial–interglacial and millennial-scale variations in the atmospheric nitrous oxide concentration during the last 800,000 years. *Quat. Sci. Rev.* **29**, 182–192 (2010).
- Capron, E. *et al.* Synchronising EDML and NorthGRIP ice cores using $\delta^{18}\text{O}$ of atmospheric oxygen ($\delta^{18}\text{O}_{\text{atm}}$) and CH_4 measurements over MIS5 (80–123 kyr). *Quat. Sci. Rev.* **29**, 222–234 (2010).
- Steen-Larsen, H. C. *et al.* Understanding the climatic signal in the water stable isotope records from the NEM shallow firn/ice cores in northwest Greenland. *J. Geophys. Res.* **116**, D06108, doi:10.1029/2010JD014311 (2011).
- Buchardt, S. L., Clausen, H. B., Vinther, B. M. & Dahl-Jensen, D. Investigating the past and recent $\delta^{18}\text{O}$ -accumulation relationship seen in Greenland ice cores. *Clim. Past* **8**, 2053–2059 (2012).
- Landais, A. *et al.* A tentative reconstruction of the last interglacial and glacial inception in Greenland based on new gas measurements in the Greenland Ice Core Project (GRIP) ice core. *J. Geophys. Res.* **108**, 4563, doi:10.1029/2002jd003147 (2003).
- Suwa, M., von Fischer, J. C., Bender, M. L., Landais, A. & Brook, E. J. Chronology reconstruction for the disturbed bottom section of the GISP2 and the GRIP ice cores: implications for Termination II in Greenland. *J. Geophys. Res.* **111**, D02101, doi:10.1029/2005JD006032 (2006).
- Johnsen, S. J. *et al.* Oxygen isotope and palaeotemperature records from six Greenland ice-core stations: Camp Century, Dye-3, GRIP, GISP2, Renland and NorthGRIP. *J. Quat. Sci.* **16**, 299–307 (2001).
- Ruth, U. *et al.* “EDML1”: a chronology for the EPICA deep ice core from Dronning Maud Land, Antarctica, over the last 150 000 years. *Clim. Past* **3**, 475–484 (2007).
- Caillon, N., Jouzel, J., Severinghaus, J. P., Chappellaz, J. & Blunier, T. A novel method to study the phase relationship between Antarctic and Greenland climate. *Geophys. Res. Lett.* **30**, 1899, doi:10.1029/2003GL017838 (2003).
- Chappellaz, J. *et al.* Synchronous changes in atmospheric CH_4 and Greenland climate between 40 and 8 kyr BP. *Nature* **366**, 443–445 (1993).
- Rodriguez-Morales, F. *et al.* Advanced multi-frequency radar instrumentation for polar research. *IEEE Trans. Geosci. Rem. Sens.* (in the press).
- Leuschen, C. *et al.* The CREIS radar suite for measurements of the ice sheets and sea ice during Operation Ice Bridge. *Am. Geophys. Un. Fall Meet.*, abstr. C44A-02 (2010).
- Buchardt, S. L. & Dahl-Jensen, D. At what depth is the Eemian layer expected to be found at NEM? *Ann. Glaciol.* **48**, 100–102 (2008).
- Dahl-Jensen, D. & Gundestrup, N. in *The Physical Basis of Ice Sheet Modelling* (ed. Waddington, E.) 31–43 (Proc. Vancouver Symp., August 1987, IAHS Publ. No. 170, 1987).
- Dahl-Jensen, D. & Gundestrup, N. S. Derivation of flow-law properties from borehole tilt data: discussion of the Dye 3, Camp Century, and Byrd Station bore-hole results. *Ann. Glaciol.* **12**, 200–201 (1989).
- Azuma, N. & Higashi, A. Mechanical properties of Dye 3 Greenland deep ice cores. *Ann. Glaciol.* **5**, 1–8 (1984).
- Jacka, T. H. Laboratory studies on relationships between ice crystal size and flow rate. *Cold Reg. Sci. Technol.* **10**, 31–42 (1984).
- Goujon, C., Barnola, J.-M. & Ritz, C. Modeling the densification of polar firn including heat diffusion: application to close-off characteristics and gas isotopic fractionation for Antarctica and Greenland sites. *J. Geophys. Res.* **108**, 4792, doi:10.1029/2002JD003319 (2003).
- Severinghaus, J. P., Grachev, A. & Battle, M. Thermal fractionation of air in polar firn by seasonal temperature gradients. *Geochem. Geophys. Geosyst.* **2**, 1048, doi:10.1029/2000GC000146 (2001).
- Masson-Delmotte, V. *et al.* Abrupt change of Antarctic moisture origin at the end of Termination II. *Proc. Natl Acad. Sci. USA* **107**, 12091–12094 (2010).
- Stocker, T. F. & Johnsen, S. J. A minimum thermodynamic model for the bipolar seesaw. *Paleoceanography* **18**, 1087, doi:10.1029/2003PA000920 (2003).
- Pedro, J. B. *et al.* The last deglaciation: timing the bipolar seesaw. *Clim. Past* **7**, 671–683 (2011).
- Stenni, B. *et al.* Expression of the bipolar see-saw in Antarctic climate records during the last deglaciation. *Nature Geosci.* **4**, 46–49 (2011).
- Raynaud, D. *et al.* The local insolation signature of air content in Antarctic ice. A new step toward an absolute dating of ice records. *Earth Planet. Sci. Lett.* **261**, 337–349 (2007).
- Berger, A., Loutre, M. F. & Laskar, J. Stability of the astronomical frequencies over the Earth's history for paleoclimate studies. *Science* **255**, 560–566 (1992).
- van de Berg, W. J., van den Broeke, M., Ettema, J., van Meijgaard, E. & Kaspar, F. Significant contribution of insolation to Eemian melting of the Greenland ice sheet. *Nature Geosci.* **4**, 679–683 (2011).
- Raynaud, D., Chappellaz, J., Ritz, C. & Martinier, P. Air content along the Greenland Ice Core Project core: a record of surface climatic parameters and elevation in central Greenland. *J. Geophys. Res.* **102**, 26607–26613 (1997).
- Vinther, B. M. *et al.* Holocene thinning of the Greenland ice sheet. *Nature* **461**, 385–388 (2009).
- Bamber, J. L., Layberry, R. L. & Gogineni, S. A new ice thickness and bed data set for the Greenland ice sheet 1. Measurement, data reduction, and errors. *J. Geophys. Res.* **106**, 33773–33780 (2001).
- Huybrechts, P., Rybak, O., Pattyn, F., Ruth, U. & Steinhage, D. Ice thinning, upstream advection, and non-climatic biases for the upper 89% of the EDML ice core from a nested model of the Antarctic ice sheet. *Clim. Past* **3**, 577–589 (2007).
- Buchardt, S. L. *Basal Melting and Eemian Ice Along the Main Ice Ridge in Northern Greenland*. Thesis, Univ. Copenhagen (2009); available at http://www.iceandclimate.nbi.ku.dk/publications/theses/PhD_Buchardt.pdf/.
- Otto-Bliesner, B. L. *et al.* Simulating arctic climate warmth and icefield retreat in the last interglaciation. *Science* **311**, 1751–1753 (2006).
- Lunt, D. J. *et al.* A multi-model assessment of last interglacial temperatures. *Clim. Past Discuss.* **8**, 3657–3691 (2012).
- Axford, Y. *et al.* Chironomids record terrestrial temperature changes throughout Arctic interglacials of the past 200,000 yr. *Geol. Soc. Am. Bull.* **123**, 1275–1287 (2011).
- Francis, D. R., Wolfe, A. P., Walker, I. R. & Miller, G. F. Interglacial and Holocene temperature reconstructions based on midge remains in sediments of two lakes from Baffin Island, Nunavut, Arctic Canada. *Palaeogeogr. Palaeoclimatol. Palaeoecol.* **236**, 107–124 (2006).
- Turney, C. S. M. & Jones, R. T. Does the Agulhas Current amplify global temperatures during super-interglacials? *J. Quat. Sci.* **25**, 839–843 (2010).
- Born, A. & Nisancioglu, K. H. Melting of Northern Greenland during the last interglacial. *Cryosphere Discuss.* **5**, 3517–3539 (2011).
- Masson-Delmotte, V. *et al.* Sensitivity of interglacial Greenland temperature and $\delta^{18}\text{O}$: ice core data, orbital and increased CO_2 climate simulations. *Clim. Past* **7**, 1041–1059 (2011).
- Masson-Delmotte, V. *et al.* EPICA Dome C record of glacial and interglacial intensities. *Quat. Sci. Rev.* **29**, 113–128 (2010).
- Kopp, R. E., Simons, F. J., Mitrovica, J. X., Maloof, A. C. & Oppenheimer, M. Probabilistic assessment of sea level during the last interglacial stage. *Nature* **462**, 863–867 (2009).
- Dutton, A. & Lambeck, K. Ice volume and sea level during the last interglacial. *Science* **337**, 216–219 (2012).
- Dahl-Jensen, D. *et al.* in *Snow, Water, Ice and Permafrost in the Arctic (SWIPA): Climate Change and the Cryosphere* (ed. AMAP) Ch. 8 (Arctic Monitoring and Assessment Programme (AMAP), Oslo, 2011).
- Bradley, S. L., Siddall, M., Milne, G. A., Masson-Delmotte, V. & Wolff, E. Where might we find evidence of a Last Interglacial West Antarctic Ice Sheet collapse in Antarctic ice core records? *Glob. Planet. Change* **88–89**, 64–75 (2012).
- Bell, R. E. *et al.* Widespread persistent thickening of the East Antarctic Ice Sheet by freezing from the base. *Science* **331**, 1592–1595 (2011).
- Raynaud, D. & Lebel, B. Total gas content and surface elevation of polar ice sheets. *Nature* **281**, 289–291 (1979).
- Martinier, P. *et al.* Air content paleo record in the Vostok ice core (Antarctica): a mixed record of climatic and glaciological parameters. *J. Geophys. Res.* **99**, 10565–10576 (1994).

Supplementary Information is available in the online version of the paper.

Acknowledgements We thank the many persons involved in logistics, drill developments and drilling, and ice-core processing and analysis in the field and in our laboratories. NEM is directed and organized by the Centre of Ice and Climate at the Niels Bohr Institute and US NSF, Office of Polar Programs. It is supported by funding agencies and institutions in Belgium (FNRS-CFB and FWO), Canada (NRC/GSC), China (CAS), Denmark (FIST), France (IPEV, CNRS/INSU, CEA and ANR), Germany (AWI), Iceland (Rannls), Japan (NIPR), South Korea (KOPRI), The Netherlands (NWO/ALW), Sweden (VR), Switzerland (SNF), the United Kingdom (NERC) and the USA (US NSF, Office of Polar Programs) and the EU Seventh Framework programmes Past4Future and Waterunderthelce. NASA is acknowledged for the OIB 2011 programme.

Author Contributions All authors contributed to the discussions that led to the results presented in the paper. M.R.A., A.-M.B., C.B., K. Keegan, P.M., S.B.S. and E.W. performed analysis and interpretation of the firm processes; A.A., D.B.-C., M. Baumgartner, M. Bigler, T. Blunier, E.J.B., E.C., J. Chappellaz, J. Chung, O.E., H.F., L.G.F., G.G., V.G., K.G.-A., M.H., Y.I., T.J., T.R.J., J.J., K. Kawamura, E.K., H.A.K., T.K., A.L., D.L., V.L., O.J.M., V.M.-D.,

J.R.M., O.M., R. Muscheler, J.-R.P., K.P., G.P., T.P., M.P., D.R., C.R., T.R., J.L.R., M.R., C.J.S., A.S., J.S., S. Schüpbach, J. P. Severinghaus, T.S., P.S., T.F.S., C.S., W.T.S., A.S.S., A. Sveinbjörnsdóttir, A. Svensson, J.U., P.V., G.v.d.W., B.H.V., B.V., A.W. and F.W. were involved in the data measurements described in detail in Supplementary Information; N.A., T. Binder, S.K., A.M., M.M.-R., D.S., E.W. and I.W. contributed to the understanding of ice rheology; J.C.B. and A.M.Z.S. investigated the biology of the ice cores; S.L.B., P.H., M.K., F.P., A.Q., C.R., O.R., A.M.S. and R.S.W.v.d.W. produced ice-sheet models; H.B.C., S.M.D., D.A.F., A.G., H.G., M.G., S.J.J., P.K., A.L., T.L., M.L., S.O.R., I.S., J. P. Steffensen and M.W. participated in the dating of the NEEM ice core; I.C., P.D., P.L.L. and J.S. produced atmosphere models; D.D.-J. analysed the data; J.W.C.W. and E.W.W. put the discussion into the text; S.G., N.B.K., C.L., J.L., J.P., C. P. and D.S. participated in obtaining and interpreting the RES images; S.B.H. and S.S. were the chief mechanic and electronic engineer on the deep ice-core drill; M.G., S.H., S.D.H., H.M., R. Mulvaney, J.R. and C.X. participated in the planning of the NEEM project; L.B.L. and C.S.H. used a GPS net to determine the surface velocities; E.C., A.L., A.J.O., F.P., H.C.S.-L., K.S. and J.Z. participated in measuring temperatures and isotopes in the firn and air; J.-L.T. was involved in the interpretation of the basal ice.

Author Information Reprints and permissions information is available at www.nature.com/reprints. The authors declare no competing financial interests. Readers are welcome to comment on the online version of the paper. Correspondence and requests for materials should be addressed to D.D.-J. (ddj@gfy.ku.dk).

NEEM community members

D. Dahl-Jensen¹, M. R. Albert², A. Aldahan^{3†}, N. Azuma⁴, D. Balslev-Clausen¹, M. Baumgartner⁵, A.-M. Berggren⁶, M. Bigler⁷, T. Binder⁸, T. Blunier¹, J. C. Bourgeois⁷, E. J. Brook⁸, S. L. Buchardt¹, C. Buizert^{1,8}, E. Capron^{9,10}, J. Chappellaz¹¹, J. Chung¹², H. B. Clausen¹, I. Cvijanovic¹, S. M. Davies¹³, P. Ditlevsen¹, O. Eicher⁵, H. Fischer⁵, D. A. Fisher⁷, L. G. Fleet¹⁰, G. Gfeller⁵, V. Gkinis¹⁴, S. Gogineni¹⁵, K. Goto-Azuma¹⁶, A. Grinsted¹, H. Gudlaugsdóttir¹⁷, M. Guillemin¹⁸, S. B. Hansen¹, M. Hansson¹⁸, M. Hirabayashi¹⁹, S. Hong¹⁹, S. D. Hur¹², P. Huybrechts²⁰, C. S. Hvidberg¹, Y. Iizuka^{18,26}, T. Jenk^{1†}, S. J. Johnsen¹, T. R. Jones¹⁴, J. Jouzel⁹, N. B. Karlsson¹, K. Kawamura¹⁶, K. Keegan², E. Kettner¹, S. Kipfstuhl²², H. A. Kjær¹, M. Koutnik²³, T. Kuramoto^{16,21}, P. Köhler²², T. Laepple²², A. Landais⁹, P. L. Langen¹, L. B. Larsen¹, D. Leuenberger⁵, M. Leuenberger⁵, C. Leuschen¹⁵, J. Li¹⁵, V. Lipenkov²⁴, P. Martinerie¹¹, O. J. Maselli²⁵, V. Masson-Delmotte⁹, J. R. McConnell²⁵, H. Miller²², O. Mini⁵, A. Miyamoto²⁶, M. Montagnat-Rentier¹, R. Mulvaney¹⁰, R. Muscheler²⁷, A. J. Orsi²⁸, J. Paden¹⁵, C. Pantoni¹, F. Pattyn²⁹, J.-R. Petit¹¹, K. Pol^{9,10}, T. Popp¹, G. Possnert³⁰, F. Prié⁹, M. Prokopiou³¹, A. Quiquet¹¹, S. O. Rasmussen¹, D. Raynaud¹¹, J. Ren³², C. Reutenauer¹, C. Ritz¹¹, T. Röckmann³¹, J. L. Rosen⁸, M. Rubino^{1,33}, O. Rybak²⁰, D. Samyn³⁴, C. J. Sapart³¹, A. Schilt^{5,8}, A. M. Z. Schmidt¹, J. Schwander⁵, S. Schüpbach⁵, I. Seierstad¹, J. P. Severinghaus²⁸, S. Sheldon¹, S. B. Simonsen¹, J. Sjolte^{1,27}, A. M. Solgaard¹, T. Sowers³⁴, P. Sperlich^{1†}, H. C. Steen-Larsen¹⁹, K. Steffen^{35†}, J. P. Steffensen¹, D. Steinhage²², T. F. Stocker⁵, C. Stowasser¹, A. S. Sturevik³, W. T. Sturges³⁶, A. Sveinbjörnsdóttir¹⁷, A. Svensson¹, J.-L. Tison²⁹, J. Uetake¹⁶, P. Vallelonga¹, R. S. W. van de Wal³¹, G. van der Wel⁵, B. H. Vaughn¹⁴, B. Vinther¹, E. Waddington²³, A. Wegner²², I. Weikusat²², J. W. C. White¹⁴, F. Wilhelms²², M. Winstrup¹, E. Witrant³⁷, E. W. Wolff¹⁰, C. Xiao^{32,38} & J. Zheng⁷

¹Centre for Ice and Climate, Niels Bohr Institute, University of Copenhagen, Juliane Maries Vej 30, 2100 Copenhagen K, Denmark. ²Thayer School of Engineering, Dartmouth University, Hanover, New Hampshire 03755, USA. ³Department of Earth Sciences, Uppsala University, Villavägen 16, 752 36 Uppsala, Sweden. ⁴Department of Mechanical

Engineering, Nagaoka University of Technology, 1603-1 Kamitomioka-machi, Nagaoka 940-2188, Japan. ⁵Climate and Environmental Physics, Physics Institute and Oeschger Centre for Climate Change Research, University of Bern, Sidlerstrasse 5, 3012 Bern, Switzerland. ⁶IWR, University of Heidelberg, Speyerer Straße 6, D-69115 Heidelberg, Germany. ⁷Natural Resources Canada, Geological Survey of Canada, 601 Booth Street, Ottawa K1A 0E8, Canada. ⁸College of Earth, Ocean, and Atmospheric Sciences, Oregon State University, 104 CEOAS Administration Building, Corvallis, Oregon 97331-5503, USA. ⁹Laboratoire des Sciences du Climat et de l'Environnement, CEA-CNRS-UVSQ, IPSL, Bâtiment 701 L'Orme des Merisiers, CEA Saclay, 91 191 Gif sur Yvette, France. ¹⁰British Antarctic Survey, Madingley Road, Cambridge CB3 0ET, UK. ¹¹LGGE, UJF-Grenoble 1, CNRS, 64 rue Molière, BP 96, 38402 St Martin d'Hères, France. ¹²Korea Polar Research Institute, Songdo Techno Park, 7-50, Songdo-dong, Yeonsu-gu, Incheon 406-840, South Korea. ¹³Department of Geography, College of Science, Swansea University, Singleton Park, Swansea SA2 8PP, UK. ¹⁴INSTAAR, University of Colorado, Boulder, Colorado 80309, USA. ¹⁵CRISIS, University of Kansas, Nichols Hall, 2335 Irving Hill Road, Lawrence, Kansas 66045, USA. ¹⁶National Institute of Polar Research, 10-3 Midori-cho, Tachikawa, Tokyo 190-8518, Japan. ¹⁷Institute of Earth and Sciences, University of Iceland, Sturlugata 7, IS-107, Reykjavik, Iceland. ¹⁸Department of Physical Geography and Quaternary Geology, Stockholm University, S-106 91 Stockholm, Sweden. ¹⁹Department of Ocean Sciences, Inha University, 100 Inha-ro, Nam-gu, Incheon 402-751, South Korea. ²⁰Earth System Sciences and Department of Geography, Vrije Universiteit Brussel, Pleinlaan 2, B-1050 Brussels, Belgium. ²¹Institute of Mountain Science, Shinshu University, 3-1-1, Asahi, Matsumoto City 390-8621, Japan. ²²Alfred Wegener Institute for Polar and Marine Research, PO Box 12 01 61, D-27515 Bremerhaven, Germany. ²³Department of Earth and Space Sciences, University of Washington, Seattle, Washington 98195-1310, USA. ²⁴Arctic and Antarctic Research Institute, St Petersburg 199397, Russia. ²⁵Desert Research Institute, Nevada System of Higher Education, Reno, Nevada 89512, USA. ²⁶Institute of Low Temperature Science, Hokkaido University, Sapporo 060-0819, Japan. ²⁷Department of Geology, Lund University, Sölvegatan 12, SE-22362 Lund, Sweden. ²⁸Scripps Institution of Oceanography, UC San Diego, La Jolla, California 92093, USA. ²⁹Laboratoire de Glaciologie, Université Libre de Bruxelles, CP160/03, Avenue F.D. Roosevelt 50, B-1050 Brussels, Belgium. ³⁰Tandem Laboratory, Uppsala University, Lagerhyddsvägen 1, 751 20 Uppsala, Sweden. ³¹Institute for Marine and Atmospheric Research Utrecht (IMAU), Utrecht University, Princetonplein 5, 3584 CC Utrecht, The Netherlands. ³²State Key Laboratory of Cryospheric Sciences, Cold and Arid Regions Environmental and Engineering Research Institute, Chinese Academy of Sciences, Lanzhou 730000, China. ³³Centre for Australian Weather and Climate Research, CSIRO Marine and Atmospheric Research, Aspendale, 3195 Victoria, Australia. ³⁴Earth and Environment Systems Institute, Penn State University, 2217 EES Building, University Park, Pennsylvania 16802, USA. ³⁵CIRES, University of Colorado, 216 UCB Boulder, Colorado 80309-0216, USA. ³⁶University of East Anglia, Norwich, Norfolk NR4 7TJ, UK. ³⁷UJF – Grenoble 1/CNRS, Grenoble Image Parole Signal Automatique (GIPSA-lab), UMR 5216, BP 46, 38402 St Martin d'Hères, France. ³⁸China Institute of Climate System, Chinese Academy of Meteorological Sciences, Beijing 100081, China.

†Present addresses: Department of Geology, United Arab Emirates University, Al Ain, United Arab Emirates (A.A.); Paul Scherrer Institute, OFLB/109, 5232 Villigen – PSI, Switzerland (T.J.); Max-Planck-Institute for Biogeochemistry, Hans-Knöll-Strasse 10, 07745 Jena, Germany (P.S.); Swiss Federal Research Institute WSL, Zuercherstrasse 111, CH-8903 Birmensdorf, Switzerland; Institute for Atmosphere and Climate Science (IAC), Swiss Federal Institute of Technology (ETH), Universitaetstrasse 16, CH-8092 Zurich, Switzerland; School of Architecture, Civil and Environmental Engineering (ENAC), Ecole polytechnique fédérale de Lausanne (EPFL), Station 2, CH-1015 Lausanne, Switzerland (K.S.).